Oxygen Spectroscopy and Polarization-Dependent Imaging Contrast (PIC)-Mapping of Calcium Carbonate Minerals and Biominerals

Ross T. DeVol,[†] Rebecca A. Metzler,[‡] Lee Kabalah-Amitai,[§] Boaz Pokroy,[§] Yael Politi,[‖,⊥] Assaf Gal,[‖] Lia Addadi,[‖] Steve Weiner,[‖] Alejandro Fernandez-Martinez,[#] Raffaella Demichelis,[▽] Julian D. Gale,[▽] Johannes Ihli,[¶] Fiona C. Meldrum,[¶] Adam Z. Blonsky,[†] Christopher E. Killian,[†] C. B. Salling,[†] Anthony T. Young,[○] Matthew A. Marcus,[○] Andreas Scholl,[○] Andrew Doran,[○] Catherine Jenkins,[○] Hans A. Bechtel,[○] and Pupa U. P. A. Gilbert*,[†,◆]

[†]Department of Physics, University of Wisconsin−Madison, 1150 University Avenue, Madison, Wisconsin 53706, United States

[‡]Department of Physics and Astronomy, Colgate University, Hamilton, New York 13346, United States

[§]Department of Materials Science & Engineering and the Russell Berrie Nanotechnology Institute, Technion - Israel Institute of Technology, Haifa 32000, Israel

[‖]Department of Structural Biology, Faculty of Chemistry, Weizmann Institute of Science, Rehovot, Israel

[#]ISTerre, CNRS & Université Grenoble Alpes, 38041 Grenoble, France

[▽]Nanochemistry Research Institute, Department of Chemistry, Curtin University, PO Box U1987, Perth, WA 6845, Australia

[¶]School of Chemistry, University of Leeds, Leeds LS2 9JT, United Kingdom

[○]Advanced Light Source, Lawrence Berkeley National Laboratory, 1 Cyclotron Road, Berkeley, California 94720, United States

[◆]Department of Chemistry, University of Wisconsin−Madison, 1101 University Avenue, Madison, Wisconsin 53706, United States

S *Supporting Information*

ABSTRACT: X-ray absorption near-edge structure (XANES) spectroscopy and spectromicroscopy have been extensively used to characterize biominerals. Using either Ca or C spectra, unique information has been obtained regarding amorphous biominerals and nanocrystal orientations. Building on these results, we demonstrate that recording XANES spectra of calcium carbonate at the oxygen K-edge enables polarization-dependent imaging contrast (PIC) mapping with unprecedented contrast, signal-to-noise ratio, and magnification. O and Ca spectra are presented for six calcium carbonate minerals: aragonite, calcite, vaterite, monohydrocalcite, and both hydrated and anhydrous amorphous calcium carbonate. The crystalline minerals reveal excellent agreement of the extent and direction of polarization dependences in simulated and experimental XANES spectra due to X-ray linear dichroism. This effect is particularly strong for aragonite, calcite, and vaterite. In natural biominerals, oxygen PIC-mapping generated high-magnification maps of unprecedented clarity from nacre and prismatic structures and their interface in *Mytilus californianus* shells. These maps revealed blocky aragonite crystals at the nacre−prismatic boundary and the narrowest calcite needle-prisms. In the tunic spicules of *Herdmania momus*, O PIC-mapping revealed the size and arrangement of some of the largest vaterite single crystals known. O spectroscopy therefore enables the simultaneous measurement of chemical and orientational information in $CaCO_3$ biominerals and is thus a powerful means for analyzing these and other complex materials. As described here, PIC-mapping and spectroscopy at the O K-edge are methods for gathering valuable data that can be carried out using spectromicroscopy beamlines at most synchrotrons without the expense of additional equipment.
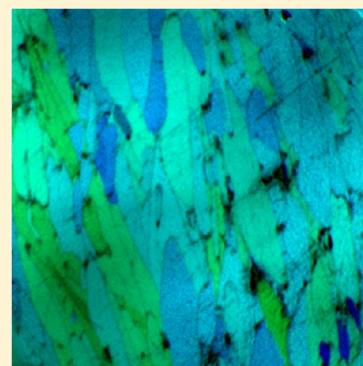
INTRODUCTION

Mollusk and foraminifera shells, eggshells, plant cystoliths, corals, sea urchin spines, and tunicate spicules are a few examples of the myriad of biominerals formed from calcium carbonate ($CaCO_3$).[1] The mechanisms by which organisms generate such biominerals have been the subject of considerable interest, due in part to the potential to translate these methods to synthetic materials.[2] One of the most powerful experimental methods used to study biominerals and their formation has proven to be spectroscopy and spectromicroscopy based on
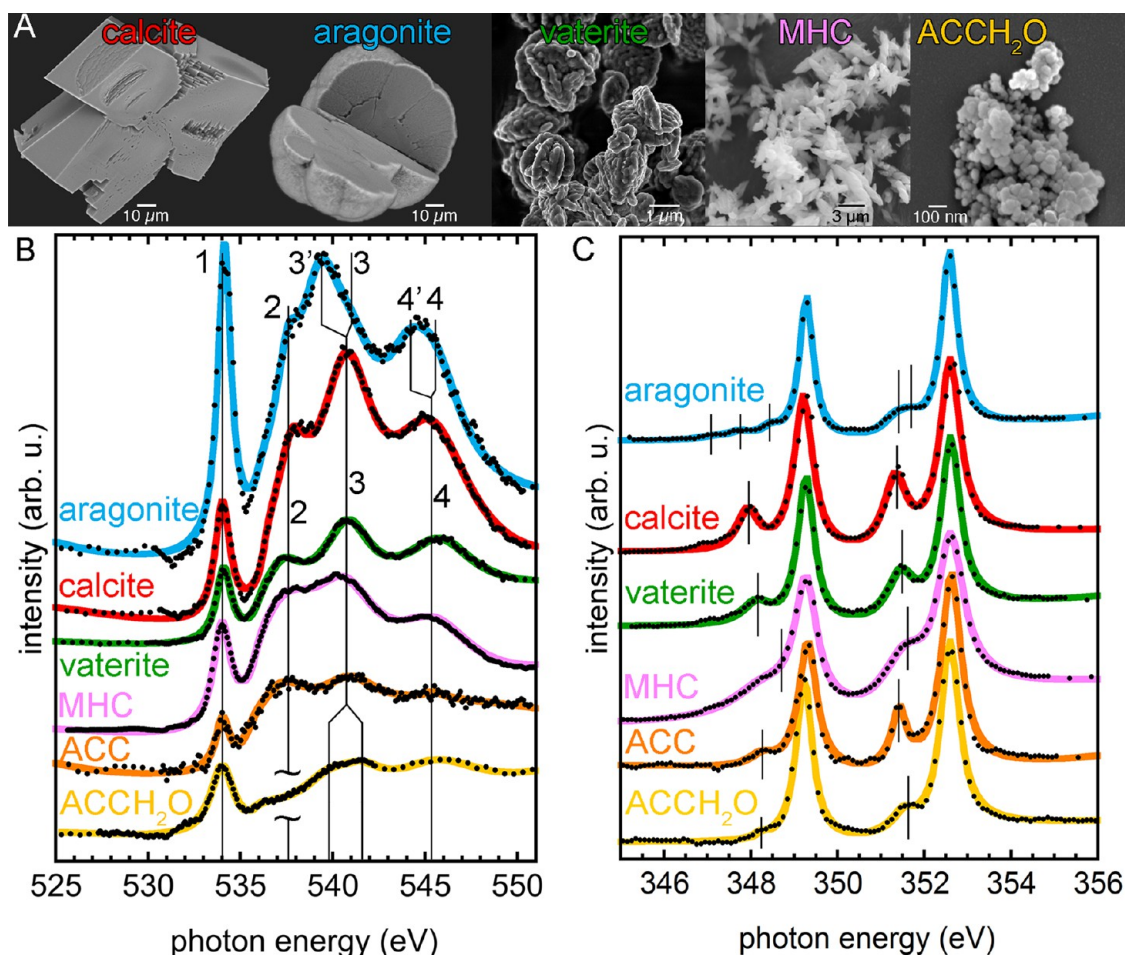
X-ray absorption near-edge structure (XANES).[3] For $CaCO_3$, this analysis has been performed at the Ca K-edge,[4] Ca L-edge,[5] and C K-edge, where in the latter case the XANES spectrum was demonstrated to vary according to the crystal orientation.

Figure 1. (A) Scanning electron micrographs of all the synthesized minerals analyzed in this work: calcite, aragonite, vaterite, monohydrocalcite (MHC), and hydrated amorphous calcium carbonate (ACC-H_2O). (B) Oxygen K-edge spectra for the five synthetic minerals in A plus biogenic ACC from a sea urchin spicule extracted from a *Strongylocentrotus purpuratus* embryo, prepared and analyzed as in Gong et al. 2012.[5f] The ACC-H_2O O spectrum is normalized to the beamline throughput intensity at each energy (I_o), whereas the ACC spectrum was normalized to a simultaneously acquired spectrum from an epoxy I_o region. The other crystalline carbonate O spectra were obtained by averaging two spectra collected with linear polarization vertical and horizontal and previously normalized to an epoxy I_o region. All spectra were scaled so that the post- and pre-edge are at 1 and 0, respectively, and displaced vertically for clarity. The solid lines are the results of peak-fitting, whereas the experimental data are displayed as black data points. Notice that for aragonite there are six Lorentzian peaks, whereas for all other minerals there are four. (C) Calcium L-edge experimental spectra from the same six minerals, distinct from one another at the crystal field peaks, indicated by vertical lines. All Ca spectra are scaled so that the most intense L_2 peak is 1 and the pre-edge is 0, and displaced vertically for clarity. All peak-fitting parameters for O and Ca spectra are presented in Tables S1 and S2 of the Supporting Information. All text-file spectra are available to the reader as Supporting Information.

This dependence was first observed in the polymorph aragonite[6] then in calcite minerals and biominerals,[5c,d,7] but it has not previously been observed in vaterite.

This orientation dependence of the XANES spectrum is due to X-ray linear dichroism, a physical effect that generates dramatic spectral differences due to changes in the carbonate group orientation with respect to the polarization of the illuminating X-rays.[8] This effect lies at the heart of the imaging method polarization-dependent imaging contrast (PIC) mapping,[5c–e,6,7,9] in which the orientations of crystals are displayed by different gray levels. In the case of calcium carbonate, the carbonate groups lie in only a few distinct orientations in a crystal, and these are repeated periodically in three dimensions to generate the entire lattice. The linear dichroism effect is therefore strongly amplified in crystals, and PIC-mapping takes full advantage of such amplification. We emphasize that this technique is just as effective for synthetic, geologic, or biogenic carbonate crystals because they all share the same crystal structure, spectral line shape, and polarization dependence.[9b] This method is analogous to pleochroism,[10] which

is widely used in optical microscopy of minerals to determine their orientation, but it is complementary to it because of higher spatial resolution, down to 20 nm.[11]

We present the first oxygen K-edge XANES spectroscopy of all the stable synthetic calcium carbonate minerals and biominerals. Previous O spectroscopy was published recently for a generic $CaCO_3$,[12] as well as for $MnCO_3$ and $FeCO_3$.[13] Our results show that O spectroscopy can be used to provide simultaneous chemical and orientational information on $CaCO_3$ biominerals and that the differences in the O spectra are significant enough to enable the different carbonate polymorphs to be distinguished in unknown specimens. The polarization dependence was also studied in detail, and it was found that X-ray linear dichroism makes the polarization-dependent contrast at the O K-edge three times greater than that at the C K-edge; this effect is strong in calcite, aragonite, and vaterite (all $CaCO_3$). For completeness, we also include in this analysis the spectra for monohydrocalcite (MHC, $CaCO_3 \cdot H_2O$) and both anhydrous and hydrated amorphous calcium carbonate (ACC and ACC-H_2O, respectively).

8450

dx.doi.org/10.1021/jp503700g | J. Phys. Chem. B 2014, 118, 8449−8457
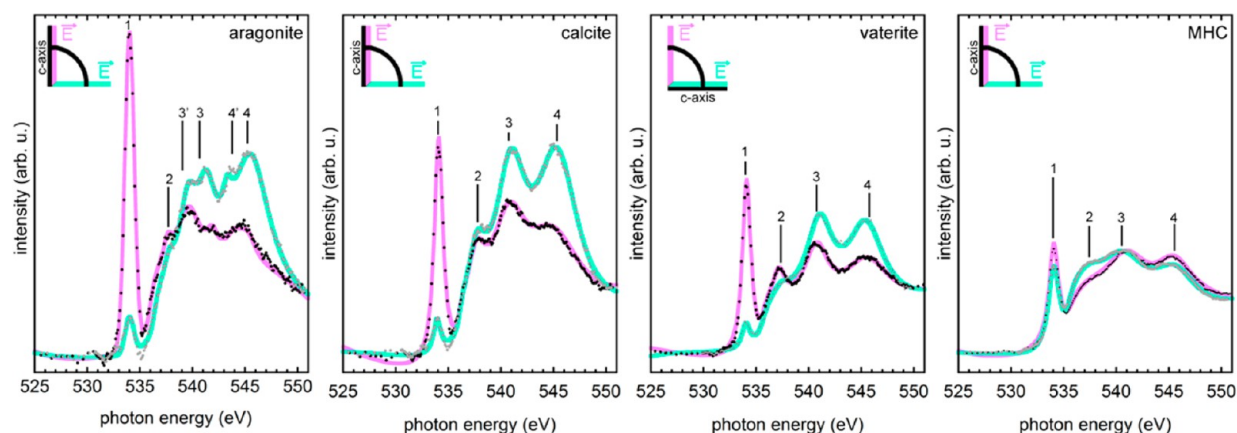
Figure 2. Polarization dependence of the O spectra in the three crystalline polymorphs of $CaCO_3$ and MHC. In each plot, the linear polarization vector ($\vec{E}$) of the illuminating X-rays is either parallel or perpendicular to the crystallographic *c*-axis, and each plot shows the spectra acquired with vertical and horizontal polarization. All spectra are normalized to the nonpolarization-dependent epoxy curve acquired simultaneously at each polarization and are scaled so that the post- and pre-edge intensities are 1 and 0, respectively. They are all plotted with the same vertical scale, such that the magnitude of the polarization dependence of each mineral can be appreciated. The greatest variation with linear polarization rotation is observed for aragonite, then calcite, vaterite, and most weakly for MHC. Notice that in all spectra, peak 1 is a π^* peak, peaks 3 and 4 are σ^* peaks anticorrelated with π^* peak 1. The peak numbers are positioned as in the spectra of Figure 1B and Table S1 of the Supporting Information.
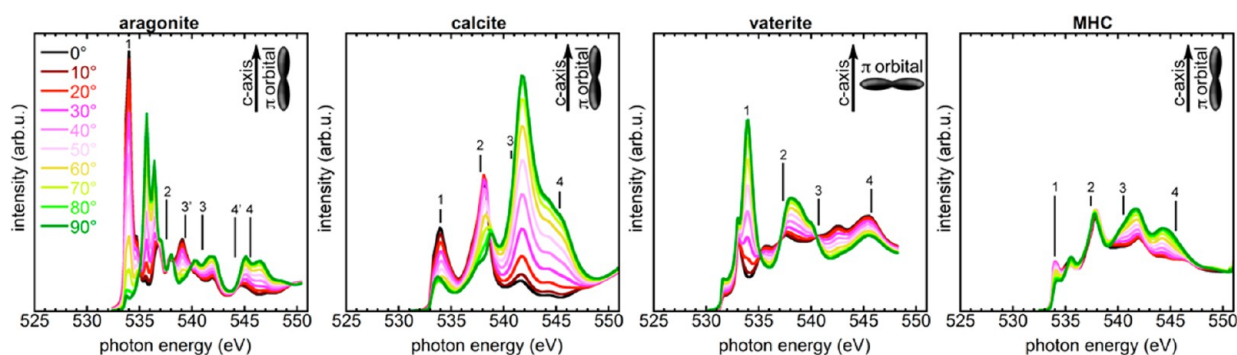
Figure 3. FEFF-simulated spectra for all four crystalline minerals. In all of these the crystal *c*-axis is vertical, and the orientation of the linear polarization $\vec{E}$ varies between vertical ($\theta = 0°$, black) and horizontal ($\theta = 90°$, green) in 10° increments. Each plot also shows the energy positions of the experimental peaks, and their labels are as in Figures 1 and 2 and Table S1 of the Supporting Information. Notice that, despite the dissimilarity in line shape and peak positions between these simulated spectra and the experimental ones shown in Figure 2, for all minerals the π^* and σ^* peaks (1, 3, 4) exhibit anticorrelated behavior as in the experimental spectra. Remarkably, in calcite and aragonite the π^* peak is at a maximum at $\theta = 0°$, whereas in vaterite the π^* peak is at a maximum at $\theta = 90°$. This is entirely consistent with the structures of these crystals. All four sets of spectra are plotted on the same vertical axis, such that the extent of their polarization dependence variation is clearly visible. All structural data (in cif format) and text files containing the inputs for the calculation of FEFF spectra (feff.inp) required to reproduce these simulations are available to the reader as Supporting Information.

MHC is rarely observed in biominerals,[14] whereas ACC-H_2O is the form of all stable biogenic amorphous calcium carbonate (plant cystoliths, crustacean cuticles, ascidian spicules, etc.[15]), is a precursor phase in sea urchin spicules and spines,[16] and most recently was mapped with 20 nm resolution using spectromicroscopy at the Ca L-edge.[5b,c,f]

■ RESULTS

In Figure 1 we present XANES spectra at the oxygen K-edge of six synthetic and biogenic calcium carbonate minerals. Ikaite ($CaCO_3 \cdot 6H_2O$) is not included as it rapidly recrystallizes to calcite at room temperature. We also acquired Ca L-edge spectra before and after each O spectrum to confirm the assignment of each mineral[5b,7b,17] and to rule out radiation damage effects. This is particularly relevant for ACC-H_2O, which transforms into anhydrous ACC and then into calcite upon X-ray exposure.[5f] Figure S1 of the Supporting Information shows the Ca spectra acquired from the same pixels as for the O spectrum of ACC-H_2O and ACC in Figure 1. All other O spectra in Figure 1 were

obtained by averaging two spectra acquired with vertical and horizontal linear polarization, to minimize polarization dependence.

At first glance, the O spectra in Figure 1 look similar to one another, apparently having four peaks, which have been labeled 1 through 4. However, significant differences can be found with careful inspection and further analysis. Notice in particular that for aragonite, peaks 3 and 4 are double-peaks such that there are six peaks rather than four. Of these, only five are evident in Figure 1, whereas all six are evident upon changes in the linear polarization, as shown in Figure 2.

Carbonate groups are trigonal planar (D_{3h} point group), with carbon lying at the center and the three oxygen atoms at the corners of the triangle. The 2p orbitals of each O atom, which combine with the 2p orbitals of C to form the π orbitals of carbonate, are perpendicular to the plane of the triangles. These triangles are displayed in red in the animated structures of all of the crystals shown in Movies M1−M4 of the Supporting Information. Hereafter we refer to the direction of the π states as
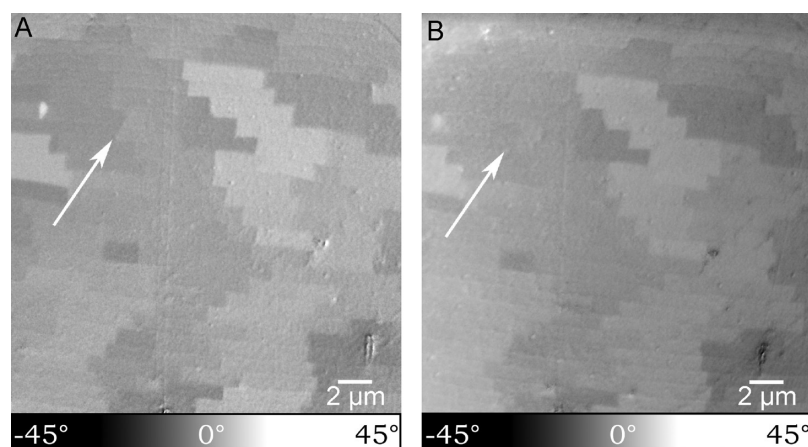
Figure 4. PIC-maps of aragonite nacre from a *Mytilus californianus* shell embedded, polished, coated,[24−26] and imaged in cross-section. (A) PIC-map at the O K-edge. Notice the staggered co-oriented tablets, revealed by similar gray levels. This map is enabled by the polarization dependence of O spectra in Figures 2 and 3. (B) PIC-map of the same region as in A but acquired at the C K-edge, as in most previous PIC-maps. The signal/noise ratio for O is three times greater than that for C; hence, the contrast and pixel resolution achievable are both greater at the O K-edge. White arrows, identically positioned in the two maps, point to the contrast between adjacent nacre tablets, which is visible in the O but not in the C PIC-map. Quantitative analysis of contrast is provided in Figure S3 of the Supporting Information.

a vector; this corresponds to the principal axis of the electron density, which is orthogonal to the red triangles. In Figure 2, if the polarization vector is parallel to the π orbitals, the O 1s → π^* C=O transition signal, which is hereafter referred to as a π^* peak, is maximal and the O 1s → σ^* C=O absorptions, or σ^* peaks, are minimal. The π^* and σ^* peaks are always anticorrelated.

In Figure 1, the vaterite and calcite O spectra are surprisingly similar, with the exception of a small shift of peak 2. In Figure 2, the most remarkable spectral behavior is observed for the π^* peak 1 in aragonite and calcite, which is at a maximum at $\theta = 0°$, whereas in vaterite the π^* peak is at a maximum at $\theta = 90°$. This is entirely consistent with the structures of these crystals and is observed in experimental and simulated spectra of Figures 2 and 3.

Peak 2 behaves differently across crystals: in calcite and MHC, peak 2 is anticorrelated with peak 1; in vaterite it is correlated with peak 1; and in aragonite, the intensity of peak 2 is nearly polarization-independent. Peak 2 is sharper in calcite and vaterite compared to that in aragonite, MHC, ACC, or ACC-H$_2$O. We suspected that O−Ca interactions are important to peak 2, as the same crystals with a sharp peak 2 also have a sharp crystal field peak at the pre-edge of the Ca L-edge spectra (Figure 1). We tested this hypothesis by running simulations of an artificial calcite structure in which all Ca atoms are replaced by Be. The results, displayed in Figure S2 of the Supporting Information, show that peak 2 disappears; hence, it must be generated by O−Ca interactions in all carbonates. Its polarization dependence in MHC (Figure 2) must be due to the orientation of O−Ca bonds. Peak 2, therefore, should not be considered either a carbonate group π^* or a σ^* peak.

The spectra in Figure 3 were simulated using multiple-scattering calculations and muffin-tin potentials in the code FEFF 9,[18] hereafter referred to as FEFF, based on structures from the literature for the four crystals aragonite,[19] calcite,[20] vaterite,[21] and MHC.[22] For vaterite, we decided to use the hexagonal structure proposed by Kamhi,[21] which includes partial occupancy of the carbonate sites, so that the spectra can be computed from a single structure. It has been recently shown that vaterite is composed of multiple structures.[23] However, this is unlikely to substantially alter the computed spectra.

In calcite and aragonite, the carbon and oxygen 2p-π orbitals in CO$_3^{2-}$ are parallel to the *c*-axis, whereas in vaterite they are perpendicular to the *c*-axis and to the sides of a hexagon whose

normal is the *c*-axis. This is clearly visible in Movies M1−M4 of the Supporting Information, where the carbonate groups are represented as red triangles and the π orbitals are perpendicular to the triangles. Hence, for calcite and vaterite, the π^* peaks are maximized when the polarization is parallel or perpendicular to the *c*-axis, respectively. This is clearly seen in the experimental and simulated spectra of Figures 2 and 3.

In MHC, there are nine distinct orientations of the carbonate groups, generated by symmetry from three independent carbonates, and these lie such that the vector sum of the π orbitals is smaller and parallel to the *c*-axis; therefore, the polarization dependence is weaker but in the same direction as that for calcite and aragonite (Figure S4 of the Supporting Information). This is nicely supported by the simulated spectra shown in Figure 3 and can be readily rationalized by the crystal structure shown in the Movies M1−M4 and Figure S4 of the Supporting Information.

Although the FEFF-simulated spectra in Figure 3 show a different number of peaks and thus do not resemble the experimental spectra all that closely, the essential features are in remarkable agreement: the π^* and σ^* sensitivity to polarization matches perfectly. The greatest variation with linear polarization rotation is observed for aragonite, then calcite, vaterite, and most weakly for MHC. This is in excellent accord with the experimental data shown in Figure 2.

The strong polarization-dependence of oxygen K-edge XANES spectra of aragonite, calcite, and vaterite makes the O K-edge ideally suited for polarization-dependent imaging contrast mapping. Indeed, as shown for the analysis of three biominerals in Figures 4−6, the resultant PIC-maps show unprecedented levels of contrast, signal/noise ratio, and therefore effective spatial resolution.

Figure 4A,B shows PIC-maps of the aragonite nacre from a *Mytilus californianus* shell. The observed structure is in excellent agreement with the recognized structure of this biomineral. However, a comparison of PIC-maps at the O K-edge (Figure 4A) and at the C K-edge, as shown in Figure 4B and in most previous nacre data,[6,9a,b,e] demonstrates that there is significantly greater signal and contrast when mapping at the O K-edge. Figure S3 of the Supporting Information presents quantitative analysis of these improvements.
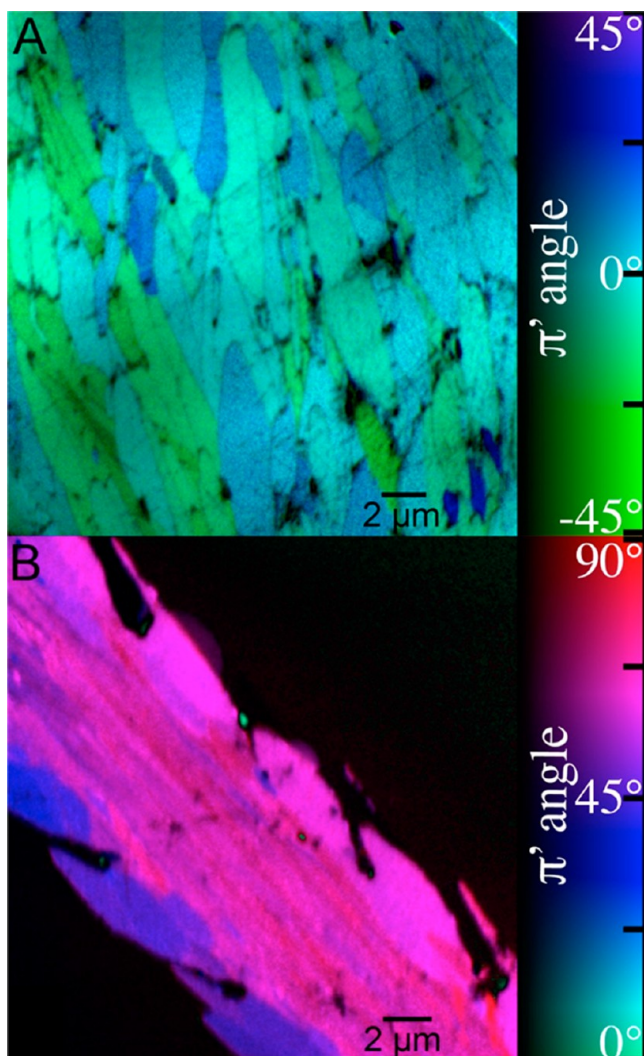
Figure 5. Color PIC-maps at the O K-edge of calcite and vaterite biominerals in cross-section,[24−26] with 20-μm field of view and 20 nm pixel size. (A) Calcite prismatic layer in a *M. californianus* shell. Notice that the variations in color, corresponding to the distribution of calcite orientation angles, reveal some of the smallest calcite prisms ever reported in any mollusk shell. (B) Vaterite tunic spicule from the tunicate *Herdmania momus*, along the diagonal of the image. Here the homogeneous color reveals the size and outline of each vaterite crystal in the spicule cross-section: these are some of the largest vaterite single crystals ever observed, exceeding 10 μm in length. Color bars for PIC-maps in A and B are shown to the right of each map and display different angle ranges to enhance color contrast between crystals. The color describes the in-plane orientation of the π orbitals in carbonate groups, and the brightness (from bright color to black) describes how far off-plane the π orbitals are. Note that the organics in A and the epoxy in B appear black because they exhibit no polarization dependence. (Figure S5 of the Supporting Information provides more details on the definition of π and π' and the color displayed.)

Compared to the nacre cross-section PIC-maps in Olson et al.,[27] the data in Figure 4 are also dramatically improved. In that earlier work the contrast was enhanced through the use of a nonlinear grayscale gradient to better display morphological differences in nacre from different species. In this work we wish to be rigorously quantitative about c'-axis orientation measurement. Hence, we do not artificially alter either the grayscale in Figure 4 or the color bars in Figures 5 and 6; they are generated as linearly varying gradients and not altered in subsequently used graphics software. When treated identically, the present O

PIC-maps are far superior, with sharper edges and greater contrast, as seen in Figure 4.

Figure 5 shows for the first time PIC-maps in color, where the color describes the orientation of carbonate groups. Furthermore, these color oxygen PIC-maps show previously unappreciated and unobserved characteristics of a calcite and a vaterite biomineral: the calcite prismatic layer in a *M. californianus* (*Mc*) shell, and vaterite tunic spicules from the tunicate *Herdmania momus*. PIC-maps show the ultrastructure of these materials with unprecedented clarity. The calcite prisms displayed in Figure 5A range in size from 0.5 to 2 μm in cross-section and are among the narrowest calcite prisms ever reported.[28] These dimensions are such that it is more appropriate to term them needle-like prisms, or needle-prisms. Such narrow needle-prisms may afford *Mc* greater resistance to wear.[7a] The vaterite crystals in the tunicate spicule in Figure 5B are among the largest vaterite single crystals ever reported, including synthetic, geologic, or biogenic vaterite.[29] These large, perfect single crystals recently facilitated a detailed structural analysis, which revealed that vaterite exhibits a double-crystal structure,[23a,30] also predicted on the basis of theoretical calculations.[23d] Figure 5B displays not only the size of homogeneously colored crystals but also their orientation with respect to one another in the pristine arrangement in the spicule, which is a result of biomineralization controlled by the *H. momus* organism. Notice that the maximum π' angular distribution observed in this entire region is within 34° ($\pm$17° angle spread footprint, not full width at half-maximum).

In low-contrast samples, greater contrast may also provide greater spatial resolution. Hence, going from the previous C PIC-mapping to the new O PIC-mapping may enable greater magnification. To test if this was the case for biominerals, we analyzed a *M. californianus* shell with an unprecedented small field of view and pixel size, 10 μm and 10 nm, respectively, and obtained satisfactory results as presented in Figure 6. The color contrast at the nacre−prismatic boundary in Figure 6A is 60° excluding the orange and purple aragonite crystals (155° including them); in Figure 6B, it is 46° excluding the outlier magenta tablet (90° including it); and in Figure 6C,D, they are 30° and 25°. The angular distribution measured at or near the boundary in nacre is much larger than ever previously observed for the *Mc* shell,[9a] but it decays to the prior value of 30° at greater distance from the nacre−prismatic boundary[9a] (Figure 6C). We note the black, purple, and orange aragonite regions at the boundary in Figure 6B, which had never been observed before. Figure S6 of the Supporting Information shows a distribution map of aragonite and calcite at a boundary region, demonstrating that the material displayed in purple and orange here is indeed aragonite but is not layered nacre. Hence, we conclude that this must be the blocky aragonite usually and somewhat erroneously[31] termed "spherulitic aragonite" at the nacre−prismatic boundary of other shells.[9a,32]

■ DISCUSSION

The advantages of using oxygen, rather than carbon, for PIC-mapping are the significantly greater signal-to-noise ratio, contrast, and therefore magnification and pixel resolution, as shown in Figure 4 and Figure S3 of the Supporting Information. These improvements are simply explained by the 3:1 ratio of [O] and [C] in carbonates. However, this means that more energy is deposited into the sample per unit area and unit time; hence, radiation damage is greater or faster. In the experiments presented, such effects were not observed, as all data were acquired before the onset of radiation damage. Another advantage is that all carbonates have distinct spectra at the O K-edge but not at the C K-edge.
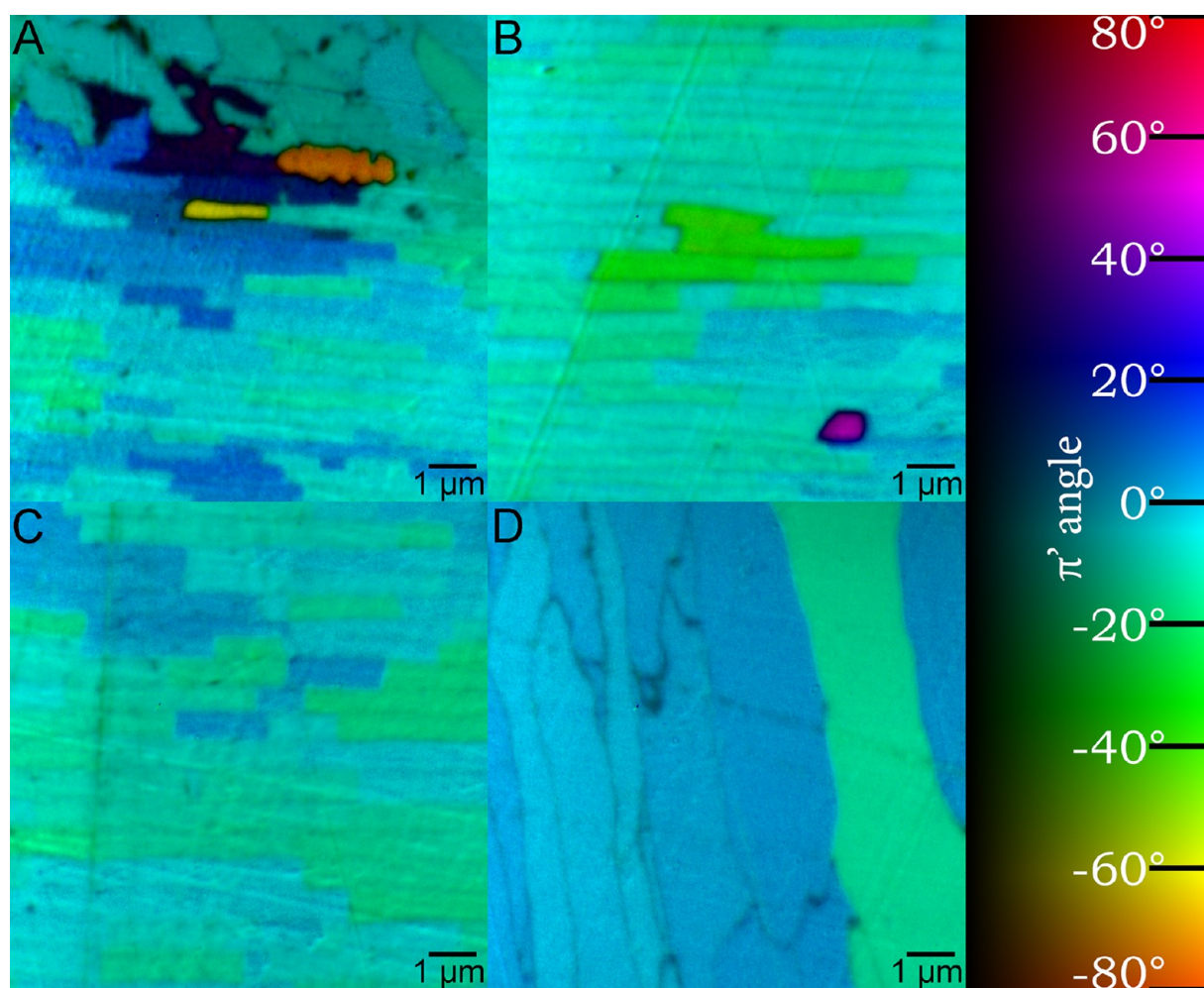
Figure 6. Color O PIC-maps with 10 μm field of view and 10 nm pixel size. All maps are from the same *M. californianus* shell (A) at the nacre−prismatic boundary, (B) in a nacre region 50 μm away from the boundary, (C) in a nacre region 110 μm away from the boundary, and (D) in the calcite prismatic layer, again showing small calcite needle-prisms. Here several needle-prisms are less than 1 μm in cross-section. The color bar is the same for all maps in A, B, C, D and displays π' angles from −80° to 80°.

Indeed, aragonite and calcite are indistinguishable at the C K-edge. The use of O rather than Ca spectroscopy does, however, have a distinct disadvantage: the O spectra are far more complex to normalize than Ca spectra, as beamline throughputs (I_o) have dips at the O K-edge due to oxygen contamination of the optics. In contrast, at the Ca L-edge, the I_o is a featureless second-order polynomial. Although at the Ca L-edge calcite, aragonite, and vaterite spectra are different from one another, MHC is similar to ACC-H_2O and differs only in the relative intensities of peaks, not in their energy positions or line shape[4a,33] (Figure 1), whereas at the O K-edge, all calcium carbonates are spectroscopically distinct. In carbonates, Ca is bonded only to O, and C is bonded only to O, whereas O is bonded to both C and Ca; this is consistent with the observed greater variability of O spectroscopy compared to that of both other elements. Furthermore, Ca does not exhibit significant dichroism.

Compared to electron back-scatter diffraction (EBSD),[34] another method to measure the orientation of nanocrystals in minerals and biominerals, PIC-mapping is equally surface sensitive, has better spatial resolution,[11] and provides data for every pixel in an image. Thus, unlike EBSD, it is not limited to those pixels that could be indexed. Unlike EBSD, however, which can resolve any crystalline structure, only dichroic crystals, that is, those with a noncubic crystal structure, can be PIC-mapped.

PIC-mapping also provides only semiquantitative orientation of the *c*-axis,[9b,35] whereas EBSD generates full 3-dimensional orientation of the *a*-, *b*-, and *c*-axes. A significant advantage of PIC-mapping over EBSD, however, and one of the salient benefits of the technique, is that it can be combined with full spectromicroscopy of the same sample region, providing elemental composition,[5e,36] redox state,[37] and electronic structure of crystalline and amorphous components alike.[5e] EBSD is of course limited to the analysis of crystalline materials.

O spectroscopy and PIC-mapping require a synchrotron, an undulator source with variable linear polarization, and a PEEM instrument. Most synchrotrons around the world have at least one, and often several such instruments, and these are typically available free of charge to any interested users, selected on the basis of scientific proposals. Therefore, we expect that both O spectroscopy and PIC-mapping will become widely used. The systems that can be analyzed with these methods not only include a wide variety of noncubic minerals and biominerals but also extend to polycrystalline metals and semiconductors or their oxides.

The first new discovery made here, that vaterite tunic spicules from *H. momus* contain large single-crystals of vaterite, is highly unexpected and significant. Previously, vaterite was observed to occur only as nanocrystals.[29d,38] The only other papers where

vaterite spicules from *H. momus* were analyzed are by Kabalah-Amitai et al.,[23a,30] but in those works the spicules had to be cut and thinned to be imaged in transmission electron microscopy. Only submicrometer fragments of spicule crystals could be analyzed; hence, the size of co-oriented crystals could not be measured. The present observation of 10 μm-single crystals of vaterite is new and paradigm-shifting, as vaterite is no longer only nano-, but microcrystalline, which represents a three-order of magnitude increase in the expected size of vaterite. The orientation of vaterite microcrystal π' angles is within a narrow distribution of 34°, which is the result of an as yet unidentified crystal growth mechanism.

The second discovery presented here is that prismatic calcite "needles" in *Mc* are smaller than 2-μm in diameter, instead of the well-known 20−50 μm diameter prisms,[39] which is in agreement with previous observations in *M. edulis* by scanning electron microscopy after weathering and separation of the prisms,[40] or directly within the pristine prismatic layer by electron back-scatter diffraction.[34f] Comparative studies of prism size and mechanical performance of the prismatic layer of mollusk shells have not yet been performed. We know that the hardness of *Mc* prismatic layer is not greater than that for other shells with larger prisms.[7a] Smaller prism width, however, may still be a significant parameter; for instance, by increasing the surface/volume ratio or the organic/inorganic concentration ratio, smaller prism width may thus confer greater fracture resistance to the host shell. Future mechanical studies will elucidate the answers to these questions.

The third discovery made here is that there is spherulitic aragonite at the nacre−prismatic boundary in *M. californianus*. These aragonite crystals are highly mis-oriented with respect to one another, but interestingly they do not seem to propagate their orientation to the adjacent nacre layers, as previously observed for many other species.[9a,17a,41]

In conclusion, we have presented oxygen K-edge spectra for three calcium carbonate polymorphs, as well as monohydrocalcite and both hydrated and anhydrous amorphous calcium carbonate, and have demonstrated excellent agreement between experimental and simulated polarization dependences for the four crystalline minerals, with some differences in line shape. For the anhydrous crystalline minerals (aragonite, calcite, and vaterite), the polarization dependence is so strong that it enables unprecedented contrast, signal-to-noise ratio, and pixel resolution in PIC-maps. Extension of this technique to the O PIC-mapping of three natural biominerals confirmed its potential for obtaining unique insights into the ultrastructures of these remarkable materials. Thus, superior images of aragonitic nacre were obtained, spherulitic aragonite in *M. californianus* was discovered, spicules that contain some of the largest single crystals of vaterite were imaged, and some of the smallest calcite needle-prism crystals yet reported were observed. Taking the potential of this method one step further, O is largely present in water and in air, in different forms including H_2O, O_2, CO_2, CO, N_2O, and NO_2, all of which have distinct spectra at the O K-edge.[42] We therefore envision that it may also be feasible to investigate the possible role of water, or even gases, in the formation of biominerals with O spectroscopy and spectromicroscopy.

ASSOCIATED CONTENT

ⓢ Supporting Information

Additional spectra; peak-fitting parameters for O and Ca spectra; detailed methods; animated rotation of the four crystal structures, each showing one unit cell with a few additional atoms added at its periphery for clarity; structural data (in cif format); text files containing the inputs for the calculation of FEFF spectra. This material is available free of charge via the Internet at http://pubs.acs.org.

■ AUTHOR INFORMATION

Corresponding Author
*Previously publishing as Gelsomina De Stasio. Phone: +1-608-262-5829. E-mail:pupa@physics.wisc.edu.

Present Address
[⊥]Y.P.: Department of Biomaterials, Max Planck Institute of Colloids and Interfaces, Potsdam, Germany.

Notes
The authors declare no competing financial interest.

■ ACKNOWLEDGMENTS

■ REFERENCES

(1) Lowenstam, H. A.; Weiner, S. *On Biomineralization*. Oxford University Press: Oxford, U.K., 1989.

(2) Meldrum, F. C.; Cölfen, H. Controlling Mineral Morphologies and Structures in Biological and Synthetic Systems. *Chem. Rev. (Washington, DC, U.S.)* **2008**, *108* (11), 4332−4432..

(3) Stöhr, J. *Nexafs Spectroscopy*. Springer: 1992; Vol. 25.

(4) (a) Levi-Kalisman, Y.; Raz, S.; Weiner, S.; Addadi, L.; Sagi, I. X-Ray Absorption Spectroscopy Studies on the Structure of a Biogenic "Amorphous" Calcium Carbonate Phase. *J. Chem. Soc.-Dalton Trans.* **2000**, No. 21, 3977−3982. (b) Politi, Y.; Levi-Kalisman, Y.; Raz, S.; Wilt, F.; Addadi, L.; Weiner, S.; Sagi, I. Structural Characterization of the Transient Amorphous Calcium Carbonate Precursor Phase in Sea Urchin Embryos. *Adv. Funct Mater.* **2006**, *16* (10), 1289−1298.

(5) (a) Benzerara, K.; Yoon, T. H.; Tyliszczak, T.; Constantz, B.; Spormann, A. M.; Brown, G. E. Scanning Transmission X-Ray Microscopy Study of Microbial Calcification. *Geobiology* **2004**, *2* (4), 249−259. (b) Politi, Y.; Metzler, R. A.; Abrecht, M.; Gilbert, B.; Wilt, F. H.; Sagi, I.; Addadi, L.; Weiner, S.; Gilbert, P. U. P. A. Transformation Mechanism of Amorphous Calcium Carbonate into Calcite in the Sea Urchin Larval Spicule. *Procs Natl. Acad. Sci. USA* **2008**, *105* (45), 17362−17366. (c) Killian, C. E.; Metzler, R. A.; Gong, Y. T.; Olson, I. C.; Aizenberg, J.; Politi, Y.; Wilt, F. H.; Scholl, A.; Young, A.; Doran, A.; et al. The Mechanism of Calcite Co-Orientation in the Sea Urchin Tooth. *J. Am. Chem. Soc.* **2009**, *131*, 18404−18409. (d) Gilbert, P. U. P. A.; Wilt, F. H., Molecular Aspects of Biomineralization of the Echinoderm Endoskeleton. In *Molecular Biomineralization*, Müller, W. E. G., Ed. Springer: Heidelberg, 2011; pp 199−223;. (e) Gilbert, P. U. P. A., Photoemission Spectromicroscopy for the Biomineralogist. In *Biomineralization Handbook, Characterization of Biominerals and Biomimetic Materials*, DiMasi, E.; Gower, L. B., Eds. CRC Press (Taylor&Francis): Boca Raton, FL, 2014;. (f) Gong, Y. U. T.; Killian, C. E.; Olson, I. C.; Appathurai, N. P.; Amasino, A. L.; Martin, M. C.; Holt, L. J.; Wilt, F. H.; Gilbert, P. U. P. A. Phase Transitions in Biogenic Amorphous Calcium Carbonate. *Proc. Natl. Acad. Sci. U. S. A.* **2012**, *109*, 6088−6093.

(6) Metzler, R. A.; Abrecht, M.; Olabisi, R. M.; Ariosa, D.; Johnson, C. J.; Frazer, B. H.; Coppersmith, S. N.; Gilbert, P. U. P. A. Architecture of Columnar Nacre, and Implications for Its Formation Mechanism. *Phys. Rev. Lett.* **2007**, *98* (26), 268102.

(7) (a) Olson, I. C.; Metzler, R. A.; Tamura, N.; Kunz, M.; Killian, C. E.; Gilbert, P. U. P. A. Crystal Lattice Tilting in Prismatic Calcite. *J. Struct Biol.* **2013**, *183*, 180−190. (b) Metzler, R. A.; Zhou, D.; Abrecht, M.; Chiou, J.-W.; Guo, J.; Ariosa, D.; Coppersmith, S. N.; Gilbert, P. U. P. A. Polarization-Dependent Imaging Contrast in Abalone Shells. *Phys. Rev. B* **2008**, *77*, 064110−1/9. (c) Brandes, J. A.; Wirick, S.; Jacobsen, C. Carbon K-Edge Spectra of Carbonate Minerals. *J. Synchrot. Radiat.* **2010**, *17*, 676−682.

(8) (a) Stohr, J.; Baberschke, K.; Jaeger, R.; Treichler, R.; Brennan, S. Orientation of Chemisorbed Molecules from Surface Absorption Fine Structure Measurements -Co and No on Ni(100). *Phys. Rev. Lett.* **1981**, *47* (5), 381−384. (b) Madix, R. J.; Solomon, J. L.; Stohr, J. The Orientation of the Carbonate Anion on Ag(110). *Surf. Sci.* **1988**, *197* (3), L253−L259.

(9) (a) Olson, I. C.; Blonsky, A. Z.; Tamura, N.; Kunz, M.; Gilbert, P. U. P. A. Crystal Nucleation and near-Epitaxial Growth in Nacre. *J. Struct Biol.* **2013**, *184*, 454−457. JOURNAL COVER (b) Olson, I. C.; Gilbert, P. U. P. A. Aragonite Crystal Orientation in Mollusk Shell Nacre May Depend on Temperature. The Angle Spread of Crystalline Aragonite Tablets Records the Water Temperature at Which Nacre Was Deposited by *Pinctada Margaritifera. Faraday Discuss.* **2012**, *159*, 421−432. (c) Killian, C. E.; Metzler, R. A.; Gong, Y. U. T.; Churchill, T. H.; Olson, I. C.; Trubetskoy, V.; Christensen, M. B.; Fournelle, J. H.; De Carlo, F.; Cohen, S.; et al. Self-Sharpening Mechanism of the Sea Urchin Tooth. *Adv. Funct Mater.* **2011**, *21*, 682−690. (d) Ma, Y. R.; Aichmayer, B.; Paris, O.; Fratzl, P.; Meibom, A.; Metzler, R. A.; Politi, Y.; Addadi, L.; Gilbert, P. U. P. A.; Weiner, S. The Grinding Tip of the Sea Urchin Tooth Exhibits Exquisite Control over Calcite Crystal Orientation and Mg Distribution. *Procs Natl. Acad. Sci. USA* **2009**, *106*, 6048−6053. (e) Metzler, R. A.; Zhou, D.; Abrecht, M.; Chiou, J. W.; Guo, J. H.; Ariosa, D.; Coppersmith, S. N.; Gilbert, P. U. P. A. Polarization-Dependent Imaging Contrast in Abalone Shells. *Phys. Rev. B* **2008**, *77* (6), 064110.

(10) Bloss, F. D. *An Introduction to the Methods of Optical Crystallography.* Holt Rinehart and Winston: 1961.

(11) Doran, A.; Church, M.; Miller, T.; Morrison, G.; Young, A. T.; Scholl, A. Cryogenic Peem at the Advanced Light Source. *J. Electr Spectrosc Rel Phenom, special issue on Photoelectron microscopy, Time-resolved pump-probe PES* **2012**, *185* (10), 340−346.

(12) Rajendran, J.; Gialanella, S.; Aswath, P. B. Xanes Analysis of Dried and Calcined Bones. *Mater. Sci. Eng. C-Mater. Biol. Appl.* **2013**, *33* (7), 3968−3979.

(13) Sherman, D. M. Electronic Structures of Siderite (Feco3) and Rhodochrosite (Mnco3): Oxygen K-Edge Spectroscopy and Hybrid Density Functional Theory. *Am. Mineral.* **2009**, *94* (1), 166−171.

(14) (a) Cailleau, G.; Braissant, O.; Dupraz, C.; Aragno, M.; Verrecchia, E. P. Biologically Induced Accumulations of Caco3 in Orthox Soils of Biga, Ivory Coast. *Catena* **2005**, *59* (1), 1−17. (b) Garvie, L. A. J. Decay-Induced Biomineralization of the Saguaro Cactus (Carnegiea Gigantea). *Am. Mineral.* **2003**, *88* (11−12), 1879−1888. (c) Señorale-Pose, M.; Chalar, C.; Dauphin, Y.; Massard, P.; Pradel, P.; Marín, M. Monohydrocalcite in Calcareous Corpuscles of *Mesocestoides Corti. Exper parasitol* **2008**, *118* (1), 54−58.

(15) Addadi, L.; Raz, S.; Weiner, S. Taking Advantage of Disorder: Amorphous Calcium Carbonate and Its Roles in Biomineralization. *Adv. Mater.* **2003**, *15* (12), 959−970.

(16) (a) Beniash, E.; Aizenberg, J.; Addadi, L.; Weiner, S. Amorphous Calcium Carbonate Transforms into Calcite During Sea Urchin Larval Spicule Growth. *Procs R Soc. B-Biol. Sci.* **1997**, *264* (1380), 461−465. (b) Politi, Y.; Arad, T.; Klein, E.; Weiner, S.; Addadi, L. Sea Urchin Spine Calcite Forms Via a Transient Amorphous Calcium Carbonate Phase. *Science* **2004**, *306* (5699), 1161−1164.

(17) (a) Metzler, R. A.; Evans, J. S.; Killian, C. E.; Zhou, D.; Churchill, T. H.; Appathurai, N. P.; Coppersmith, S. N.; Gilbert, P. U. P. A. Nacre Protein Fragment Templates Lamellar Aragonite Growth. *J. Am. Chem.*

Soc. **2010**, *132*, 6329−6334. (b) Rez, P.; Blackwell, A. Ca L-23 Spectrum in Amorphous and Crystalline Phases of Calcium Carbonate. *J. Phys. Chem. B* **2011**, *115* (38), 11193−11198.

(18) Rehr, J. J.; Deleon, J. M.; Zabinsky, S. I.; Albers, R. C. Theoretical X-Ray Absorption Fine-Structure Standards. *J. Am. Chem. Soc.* **1991**, *113* (14), 5135−5140.

(19) de Villiers, J. P. R. Crystal Structures of Aragonite, Strontianite, and Witherite. *Am. Mineral.* **1971**, *56* (5−6), 758−773.

(20) Wyckoff, R. W. G. *Crystal Structures.* Interscience publishers: New York, 1963; Vol. *1*.

(21) Kamhi, S. R. On the Structure of Vaterite Caco3. *Acta Crystallogr.* **1963**, *16* (8), 770−772.

(22) Swainson, I. P. The Structure of Monohydrocalcite and the Phase Composition of the Beachrock Deposits of Lake Butler and Lake Fellmongery, South Australia. *Am. Mineral.* **2008**, *93* (7), 1014−1018.

(23) (a) Kabalah-Amitai, L.; Mayzel, B.; Kauffmann, Y.; Fitch, A. N.; Bloch, L.; Gilbert, P. U. P. A.; Pokroy, B. Vaterite Crystals Contain Two Interspersed Crystal Sructures. *Science* **2013**, *340* (6131), 454−457. (b) Mugnaioli, E.; Andrusenko, I.; Schüler, T.; Loges, N.; Dinnebier, R. E.; Panthöfer, M.; Tremel, W.; Kolb, U. Ab Initio Structure Determination of Vaterite by Automated Electron Diffraction. *Angew. Chem., Int. Ed.* **2012**, *51* (28), 7041−7045. (c) Wang, J.; Becker, U. Structure and Carbonate Orientation of Vaterite (CaCO3). *Am. Mineral.* **2009**, *94* (2−3), 380−386. (d) Demichelis, R.; Raiteri, P.; Gale, J. D.; Dovesi, R. The Multiple Structures of Vaterite. *Cryst. Growth Des.* **2013**, *13*, 2247−2251.

(24) Gilbert, B.; Andres, R.; Perfetti, P.; Margaritondo, G.; Rempfer, G.; De Stasio, G. Charging phenomena in PEEM imaging and spectroscopy. *Ultramicroscopy* **2000**, *83*, 129.

(25) De Stasio, G.; Frazer, B. H.; Gilbert, B.; Richter, K. L.; Valley, J. W. Compensation of charging in X-PEEM: a successful test on mineral inclusions in 4.4 Ga old zircon. *Ultramicroscopy* **2003**, *98*, 57.

(26) Gilbert, P. U. P. A. In *Biomineralization Handbook, Characterization of Biominerals and Biomimetic Materials*; DiMasi, E.; Gower, L. B., Eds.; CRC Press: Boca Raton, FL, 2014, p 135.

(27) Olson, I. C.; Kozdon, R.; Valley, J. W.; Gilbert, P. U. P. A. Mollusk Shell Nacre Ultrastructure Correlates with Environmental Temperature and Pressure. *J. Am. Chem. Soc.* **2012**, *134*, 7351−7358.

(28) (a) Cusack, M.; Freer, A. Biomineralization: Elemental and Organic Influence in Carbonate Systems. *Chem. Rev. (Washington, DC, U.S.)* **2008**, *108* (11), 4433−4454. (b) Checa, A. G.; Esteban-Delgado, F. J.; Ramirez-Rico, J.; Rodriguez-Navarro, A. B. Crystallographic Reorganization of the Calcitic Prismatic Layer of Oysters. *J. Struct Biol.* **2009**, *167* (3), 261−270. (c) MacDonald, J.; Freer, A.; Cusack, M. Alignment of Crystallographic C-Axis Throughout the Four Distinct Microstructural Layers of the Oyster *Crassostrea gigas. Cryst. Growth Des.* **2010**, *10* (3), 1243−1246. (d) Okumura, T.; Suzuki, M.; Nagasawa, H.; Kogure, T. Characteristics of Biogenic Calcite in the Prismatic Layer of a Pearl Oyster, *Pinctada Fucata. Micron* **2010**, *41* (7), 821−826. (e) Suzuki, M.; Kameda, J.; Sasaki, T.; Saruwatari, K.; Nagasawa, H.; Kogure, T. Characterization of the Multilayered Shell of a Limpet, *Lottia kogamogai* (Mollusca: Patellogastropoda), Using Sem-Ebsd and Fib-Tem Techniques. *J. Struct Biol.* **2010**, *171* (2), 223−230. (f) Cusack, M.; Guo, D. J.; Chung, P.; Kamenos, N. A. Biomineral Repair of Abalone Shell Apertures. *J. Struct Biol.* **2013**, *183* (2), 165−171. (g) Cusack, M.; Parkinson, D.; Freer, A.; Perez-Huerta, A.; Fallick, A. E.; Curry, G. B. Oxygen Isotope Composition in Modiolus Modiolus Aragonite in the Context of Biological and Crystallographic Control. *Mineral. Mag.* **2008**, *72* (2), 569−577.

(29) (a) Beck, R.; Flaten, E.; Andreassen, J. P. Influence of Crystallization Conditions on the Growth of Polycrystalline Particles. *Chem. Eng. Technol.* **2011**, *34* (4), 631−638. (b) Dupont, L.; Portemer, F.; Figlarz, M. Synthesis and Study of a Well Crystallized Caco3 Vaterite Showing a New Habitus. *J. Mater. Chem.* **1997**, *7* (5), 797−800. (c) Pouget, E. M.; Bomans, P. H. H.; Dey, A.; Frederik, P. M.; de With, G.; Sommerdijk, N. The Development of Morphology and Structure in Hexagonal Vaterite. *J. Am. Chem. Soc.* **2010**, *132* (33), 11560−11565. (d) Xu, A. W.; Antonietti, M.; Colfen, H.; Fang, Y. P. Uniform Hexagonal Plates of Vaterite CaCO3 Mesocrystals Formed by

8456

dx.doi.org/10.1021/jp503700g | *J. Phys. Chem. B* 2014, 118, 8449−8457

Biomimetic Mineralization. *Adv. Funct. Mater.* **2006**, *16* (7), 903−908. (e) Schenk, A. S.; Albarracin, E. J.; Kim, Y.-Y.; Ihli, J.; Meldrum, F. C. Confinement Stabilises Single Crystal Vaterite Rods. *ChemComm* **2014**, *50*, 4729−4732.

(30) Kabalah-Amitai, L.; Mayzel, B.; Zaslansky, P.; Kauffmann, Y.; Clotens, P.; Pokroy, B. Unique Crystallographic Pattern in the Macro to Atomic Structure of Herdmania Momus Vateritic Spicules. *J. Struct Biol.* **2013**, *183* (2), 191−198.

(31) Shtukenberg, A. G.; Punin, Y. O.; Gunn, E.; Kahr, B. Spherulites. *Chem. Rev. (Washington, DC, U.S.)* **2012**, *112* (3), 1805−1838.

(32) (a) Mutvei, H., Structure of Molluscan Prismatic Shell Layers. In *Origin, Evolution, and Modern Aspects of Biomineralization in Plants and Animals*; Crick, R. E., Ed. Plenum Press: New York, 1989; pp 137−151. (b) Gilbert, P. U. P. A.; Metzler, R. A.; Zhou, D.; Scholl, A.; Doran, A.; Young, A.; Kunz, M.; Tamura, N.; Coppersmith, S. N. Gradual Ordering in Red Abalone Nacre. *J. Am. Chem. Soc.* **2008**, *130* (51), 17519−17527. (c) Mutvei, H.; Dunca, E. Crystalline Structure, Orientation and Nucleation of the Nacreous Tablets in the Cephalopod Nautilus. *Paläontologische Z.* **2010**, *84* (4), 457−465.

(33) (a) Neumann, M.; Epple, M. Monohydrocalcite and Its Relationship to Hydrated Amorphous Calcium Carbonate in Bio-minerals. *Eur. J. Inorg. Chem.* **2007**, *2007* (14), 1953−1957. (b) Lam, R. S.; Charnock, J. M.; Lennie, A.; Meldrum, F. C. Synthesis-Dependant Structural Variations in Amorphous Calcium Carbonate. *CrystEng-Comm* **2007**, *9* (12), 1226−1236. (c) Michel, F. M.; MacDonald, J.; Feng, J.; Phillips, B. L.; Ehm, L.; Tarabrella, C.; Parise, J. B.; Reeder, R. J. Structural Characteristics of Synthetic Amorphous Calcium Carbonate. *Chem. Mater.* **2008**, *20* (14), 4720−4728. (d) Cartwright, J. H.; Checa, A. G.; Gale, J. D.; Gebauer, D.; Sainz-Díaz, C. I. Calcium Carbonate Polyamorphism and Its Role in Biomineralization: How Many Amorphous Calcium Carbonates Are There? *Angew. Chem., Int. Ed.* **2012**, *51* (48), 11960−11970.

(34) (a) Dalbeck, P.; England, J.; Cusack, M.; Lee, M. R.; Fallick, A. E. Crystallography and Chemistry of the Calcium Carbonate Polymorph Switch in M. Edulis Shells. *Eur. J. Mineral.* **2006**, *18* (5), 601−609. (b) Checa, A. G.; Esteban-Delgado, F. J.; Ramirez-Rico, J.; Rodriguez-Navarro, A. B. Crystallographic Reorganization of the Calcitic Prismatic Layer of Oysters. *J. Struct. Biol.* **2009**, *167* (3), 261−270. (c) MacDonald, J.; Freer, A.; Cusack, M. Alignment of Crystallographic c-Axis throughout the Four Distinct Microstructural Layers of the Oyster *Crassostrea gigas*. *Cryst. Growth Des.* **2010**, *10* (3), 1243−1246. (d) Perez-Huerta, A.; Dauphin, Y.; Cuif, J.-P.; Cusack, M. High Resolution Electron Backscatter Diffraction (EBSD) Data from Calcite Biominerals in Recent Gastropod Shells. *Micron* **2011**, *42* (3), 246−251. (e) Schmahl, W. W.; Griesshaber, E.; Kelm, K.; Goetz, A.; Jordan, G.; Ball, A.; Xu, D. Y.; Merkel, C.; Brand, U. Hierarchical Structure of Marine Shell Biomaterials: Biomechanical Functionalization of Calcite by Brachiopods. *Z. Kristallogr. - Cryst. Mater.* **2012**, *227* (11), 793−804. (f) Griesshaber, E.; Schmahl, W. W.; Ubhi, H. S.; Huber, J.; Nindiyasari, F.; Maier, B.; Ziegler, A. Homoepitaxial Meso- and Microscale Crystal Co-Orientation and Organic Matrix Network Structure in Mytilus Edulis Nacre and Calcite. *Acta Biomater.* **2013**, *9* (12), 9492−9502.

(35) Gilbert, P. U. P. A.; Young, A.; Coppersmith, S. N. Measurement of c-Axis Angular Orientation in Calcite ($CaCO_3$) Nanocrystals Using X-Ray Absorption Spectroscopy. *Proc. Natl. Acad. Sci. U.S.A.* **2011**, *108*, 11350−11355.

(36) Gilbert, P. U. P. A.; Frazer, B. H.; Abrecht, M., The Organic-Mineral Interface in Biominerals. In *Molecular Geomicrobiology*; Banfield, J. F., Nealson, K. H., Cervini-Silva, J., Eds.; Reviews in Mineralogy and Geochemistry; Mineralogical Society of America: Washington, DC, 2005; Vol. *59*, pp 157−185.

(37) Gilbert, B.; Frazer, B. H.; Belz, A.; Conrad, P. G.; Nealson, K. H.; Haskel, D.; Lang, J. C.; Srajer, G.; De Stasio, G. Multiple Scattering Calculations of Bonding and X-Ray Absorption Spectroscopy of Manganese Oxides. *J. Phys. Chem. A* **2003**, *107* (16), 2839−2847.

(38) (a) Gehrke, N.; Colfen, H.; Pinna, N.; Antonietti, M.; Nassif, N. Superstructures of Calcium Carbonate Crystals by Oriented Attach-ment. *Cryst. Growth Des.* **2005**, *5* (4), 1317−1319. (b) Li, M.; Mann, S. Emergent Nanostructures: Water-Induced Mesoscale Transformation of Surfactant-Stabilized Amorphous Calcium Carbonate Nanoparticles in Reverse Microemulsions. *Adv. Funct. Mater.* **2002**, *12* (11−12), 773−779. (c) Rudloff, J.; Colfen, H. Superstructures of Temporarily Stabilized Nanocrystalline $CaCO_3$ Particles: Morphological Control via Water Surface Tension Variation. *Langmuir* **2004**, *20* (3), 991−996.

(39) (a) Li, H. Y.; Xin, H. L.; Kunitake, M. E.; Keene, E. C.; Muller, D. A.; Estroff, L. A. Calcite Prisms from Mollusk Shells (*Atrina rigida*): Swiss-Cheese-Like Organic-Inorganic Single-Crystal Composites. *Adv. Funct. Mater.* **2011**, *21* (11), 2028−2034. (b) Nudelman, F.; Chen, H. H.; Goldberg, H. A.; Weiner, S.; Addadi, L. Spiers Memorial Lecture: Lessons from Biomineralization: Comparing the Growth Strategies of Mollusc Shell Prismatic and Nacreous Layers in *Atrina rigida*. *Faraday Discuss.* **2007**, *136*, 9−25.

(40) Villagran, X. S.; Poch, R. M. A New Form of Needle-Fiber Calcite Produced by Physical Weathering of Shells. *Geoderma* **2014**, *213*, 173−177.

(41) Farre, B.; Brunelle, A.; Laprevote, O.; Cuff, J. P.; Williams, C. T.; Dauphin, Y. Shell Layers of the Black-Lip Pearl Oyster Pinctada Margaritifera: Matching Microstructure and Composition. *Comp. Biochem. Physiol., Part B: Biochem. Mol. Biol.* **2011**, *159* (3), 131−139.

(42) (a) Yang, B. X.; Kirz, J.; Sham, T. K. Oxygen K-Edge Absorption Spectra of O_2, Co and CO_2. *Phys. Lett. A* **1985**, *110* (6), 301−304. (b) Bergmann, U.; Wernet, P.; Glatzel, P.; Cavalleri, M.; Pettersson, L. G. M.; Nilsson, A.; Cramer, S. P. X-Ray Raman Spectroscopy at the Oxygen K Edge of Water and Ice: Implications on Local Structure Models. *Phys. Rev. B* **2002**, *66* (9), 092107. (c) Kosugi, N.; Shigemasa, E.; Yagishita, A. High-Resolution and Symmetry-Resolved Oxygen K-Edge Spectra of O_2. *Chem. Phys. Lett.* **1992**, *190* (5), 481−488. (d) Bowron, D. T.; Krisch, M. H.; Barnes, A. C.; Finney, J. L.; Kaprolat, A.; Lorenzen, M. X-Ray-Raman Scattering from the Oxygen K-Edge in Liquid and Solid H_2O. *Phys. Rev. B* **2000**, *62* (14), R9223−R9227. (e) Ceballos, G.; Wende, H.; Baberschke, K.; Arvanitis, D. Molecular Geometry Modifications Upon Adsorption for N_2O: N and O K-Edge NEXAFS. *Surf. Sci.* **2001**, *482*, 15−20.

■ NOTE ADDED AFTER ASAP PUBLICATION

This paper was published ASAP on June 10, 2014. References 24−26 were added. The revised paper was reposted on June 25, 2014.

8457

dx.doi.org/10.1021/jp503700g | *J. Phys. Chem. B* 2014, 118, 8449−8457